Dynamic history of the inner core constrained by seismic anisotropy

Daniel A Frost, Marine Lasbleis, Brian Chandler, Barbara Romanowicz

Title: Dynamic history of the inner core constrained by seismic anisotropy

Author list: Daniel A. Frost[1]*, Marine Lasbleis[23], Brian Chandler[1], Barbara Romanowicz[145]

Affiliations:
1Department of Earth & Planetary Science, University of California, Berkeley, CA, USA.
[2] Laboratoire de Planétologie et Géodynamique, UMR 6112, Université de Nantes, CNRS, France
[3]Earth-Life Science Institute, Tokyo Institute of Technology, Meguro, Tokyo 152-8551, Japan
[4] Collège de France, Paris, France.
[5] Université de Paris, Institut de Physique du Globe de Paris, Paris, France.

*Correspondence to: dafrost@berkeley.edu

Abstract

Progressive crystallisation of Earth's inner core drives convection in the outer core and magnetic field generation. Determining the rate and pattern of inner core growth is thus crucial to understanding the evolution of the geodynamo. The growth history of the inner core is likely recorded in the distribution and strength of its seismic anisotropy, which arises from deformation texturing constrained by conditions at the inner-core solid-fluid boundary. Here we show from analysis of seismic body wave travel times that the strength of seismic anisotropy increases with depth within the inner core, and the strongest anisotropy is offset from Earth's rotation axis. Then, using geodynamic growth models and mineral physics calculations, we simulate the development of inner core anisotropy in a self-consistent manner. From this we find that an inner core composed of hexagonally close-packed iron-nickel alloy, deformed by a combination of preferential equatorial growth and slow translation, can match the seismic observations without requiring hemispheres with sharp boundaries. Our model of inner core growth history is compatible with external constraints from outer core dynamics, and supports arguments for a relatively young inner core (~0.5–1.5 Ga) and a viscosity >10^{18} Pa-s.

Main text

The presence of seismic anisotropy - the dependence of seismic wavespeed on direction of propagation - in the inner core (IC) was proposed over 30 years ago to explain the early arrival times of IC sensitive seismic body waves (PKPdf) travelling on paths parallel to the Earth's rotation axis[1,2] and anomalous splitting of core-sensitive free oscillations[3]. This anisotropy is thought to result from alignment of iron crystals caused by deformation in a flow field induced by the evolution of the core, i.e. deformation texturing. Previously, different geodynamic[4] and plastic deformation mechanisms[5] were explored to explain the variation of PKPdf travel times with angle of the ray path with respect to the rotation axis. Here, we combine geodynamic modelling of flow in the IC, allowing for slow lateral translation, with present knowledge on the mineralogy and deformation mechanisms proposed for the IC to explain spatial patterns of observed seismic travel times in an updated dataset.

Indeed, early models of seismic anisotropy based on measurements of PKPdf travel times featured constant cylindrical anisotropy, with the fast axis parallel to Earth's rotation axis. Further work on IC structure has revealed increasing complexity. Recent IC models comprise two quasi-hemispheres of differing strengths of anisotropy, ~4.8% on average in the quasi-western hemisphere (WH), and ~1.4% in the quasi-eastern hemisphere (EH)[6–8]. Anisotropy strength increases with depth in the IC up to 8.8% at the centre of the IC[9]. However, past models suffer from the poor data coverage on polar paths, due to the limited distribution of earthquakes and stations.

Seismic analysis of asymmetric anisotropy

Aiming to address this issue, we have made new differential travel time measurements of PKPab-df and PKPbc-df from recent seismic deployments (Fig. 1 and Extended Data Fig. 1), increasing sampling of the IC along polar directions at a large range of depths, and added them to our existing global collection (See Methods). The updated dataset samples the IC close to Earth's rotation axis: from the inner core boundary (ICB) to within 35 km of the centre of the Earth.

Differential travel time anomalies, expressed as the effective P-velocity anomaly within the IC ($dlnV = -\frac{dT}{Tic}$, where Tic is the travel time through the IC) exhibit a strong dependence on ξ, the angle of the path within the IC relative to the rotation axis (Fig. 1a), with residuals of up to 9.9 s at the largest distances for polar paths, and ±2 s for more equatorial paths (Extended Data Fig. 2). Furthermore, the residuals depend on both the longitude and depth of the turning point of the ray (Fig. 1b,c,d). To first order, as found previously[6–9], the data exhibit hemispherical differences (Fig. 1 and Extended Data Fig. 4). Assuming a linear dependence of anisotropy on depth in each hemisphere, we determine the best fitting western boundary of the WH to be between -166°E and -159°E (Methods and Extended Data Fig. 5). However, sharp hemispherical boundaries are difficult to reconcile with geodynamic models of IC growth.

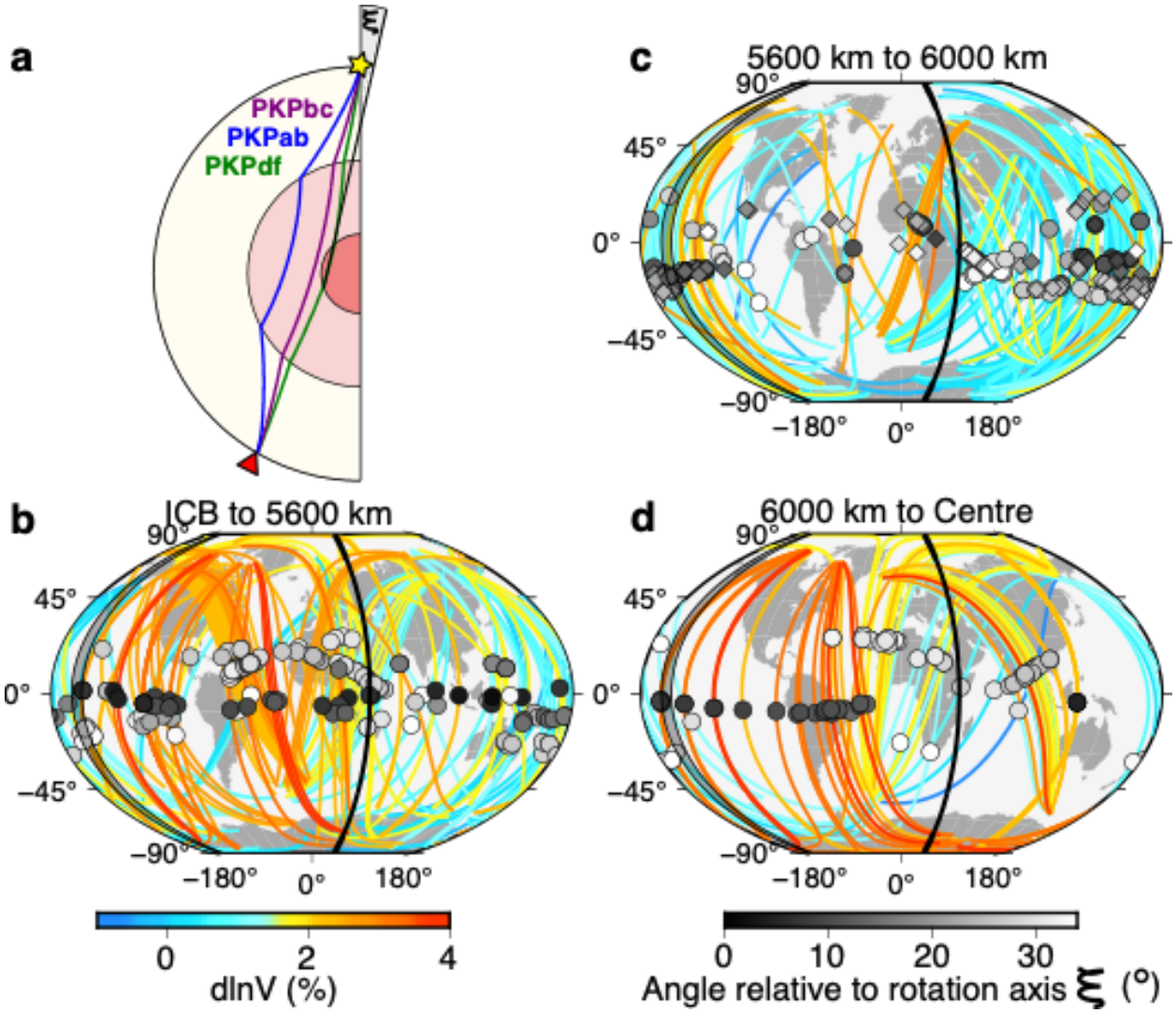

Fig. 1: Sampling of the inner core with polar PKP rays. (a) Ray paths of PKP branches used here. PKPdf samples the IC, while PKPbc and PKPab remain in the outer core. ξ is the angle that the PKPdf path in the IC makes with Earth's rotation axis. (b-d): Only polar paths (ξ<35°) from source to receiver colour-coded by effective IC velocity anomaly (line colour) and ξ (symbol colour) for paths turning between (b) 5200 and 5600 km depth, (c) 5600 km and 6000 km, and (d) 6000 km and Earth's centre. 530 polar paths are shown. Turning points for PKPbc-df and PKPab-df ray pairs are shown as diamonds and circles, respectively. We exclude the South Sandwich Islands (SSI) to Alaska paths. Grey region marks best fitting WH boundaries determined in this study and solid line marks the EH boundary[10].

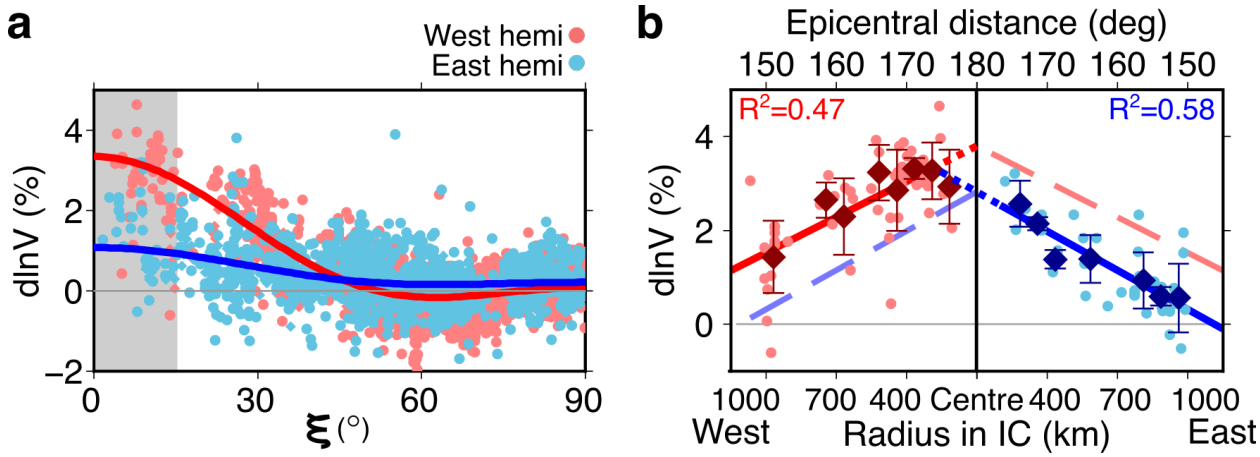

Fig. 2: Effective velocity anomaly in the inner core from PKPab-df and PKPbc-df travel time observations as a function of ξ and epicentral distance. (a) Effective velocity anomalies as a function of ξ display a hemispherical pattern implying stronger anisotropy in the WH (red) than in the EH (blue). Data from the SSI to Alaska are excluded (Extended Data Figure 3). **(b)** IC velocity anomaly as a function of epicentral distance, and thus bottoming radius of the ray in the WH (left) and EH (right), for data with ξ≤15° (shaded region in (**a**)). Solid lines mark linear fits as a function of distance in the respective hemispheres with mirror images across the centre of the Earth (180°) shown as broken lines. Moving averages (diamonds) and standard deviations at 2.5° increments in distance highlight the robust trends. The EH trend is extended to meet the WH trend (at 400 km radius) with a dotted blue line.

Examining the data more closely, we find that the effective velocity anomaly linearly increases with distance, i.e. turning point radius in the IC, in both hemispheres (Fig. 2b). The gradient with distance is approximately equal in both hemispheres, but with an offset to larger anomalies in the WH. This gradient is dependent on ξ and is steepest and most robustly defined for polar paths (0<ξ<15°) (Extended Data Fig. 6). The largest effective velocity anomalies (≥3.5% *dlnV*) are recorded in the WH, for rays bottoming at around 400 km radius (distances ≥170°) with longitude ~60°W, not at the centre of the IC. Our travel time data suggest a depth-dependence of anisotropy that, to first order, is smooth and asymmetric with respect to the centre of the Earth, rather than a hemispherical pattern with sharp boundaries between the hemispheres.

Growing anisotropic texture in the inner core

In order to interpret the seismological observations, we consider that the core likely grows preferentially at the equator due to Taylor column convection in the outer core, which induces more efficient heat transport in the cylindrically radial direction[11,12]. Isostatic adjustment would cause the oblate IC to flow inwards from the equator and up towards the poles[11,13]. Such a flow would be confined to the uppermost layer if a strong density stratification existed, and would induce deformation at depth if not[13]. Any asymmetry to the heat extraction from the IC in the plane of the equator would cause asymmetric growth[12,14] resulting in lateral advection of the growing IC and thus slow net translation. Previous studies attempted to explain the depth dependence of anisotropy by degree 2 flow[11,14] on the one hand, and the hemispherical dichotomy by degree 1 flow[15,16] on the other. However,

these hemispherical studies considered fast convective instabilities resulting in a degree 1 flow that, alone, could not produce the observed seismic anisotropy pattern and strength. Guided by our seismic observations, we combine the processes of preferred equatorial growth and hemispherically asymmetric growth and analytically model the flow pattern in a neutrally stratified IC (Fig. 3; see Methods). Advection of strained crystals along the translation axis shifts the pattern of high deformation laterally from the axis of rotation, with lateral offset of the high deformation zone from the rotation axis depending on the chosen translation rate. A key assumption here is that the translation rate is slower than the rate of growth, resulting from differential growth[14], and not from simultaneous melting and freezing on opposite hemispheres[15,16]. Given the limited constraints, the age of the IC and the translation velocity are both free parameters of such a model. The differential growth rate of the IC between the equator and the poles is described by the parameter S2, which controls the magnitude and pattern of strain experienced. S2 is loosely constrained to between 0 and 1 from dynamical arguments[11], while geodynamical models of the outer core[12,14] argue for a value of ~0.4. Constraints on S2 are not strong, however additional information can be brought in from mineral physics, which provides constraints on strain rate dependent development of anisotropy.

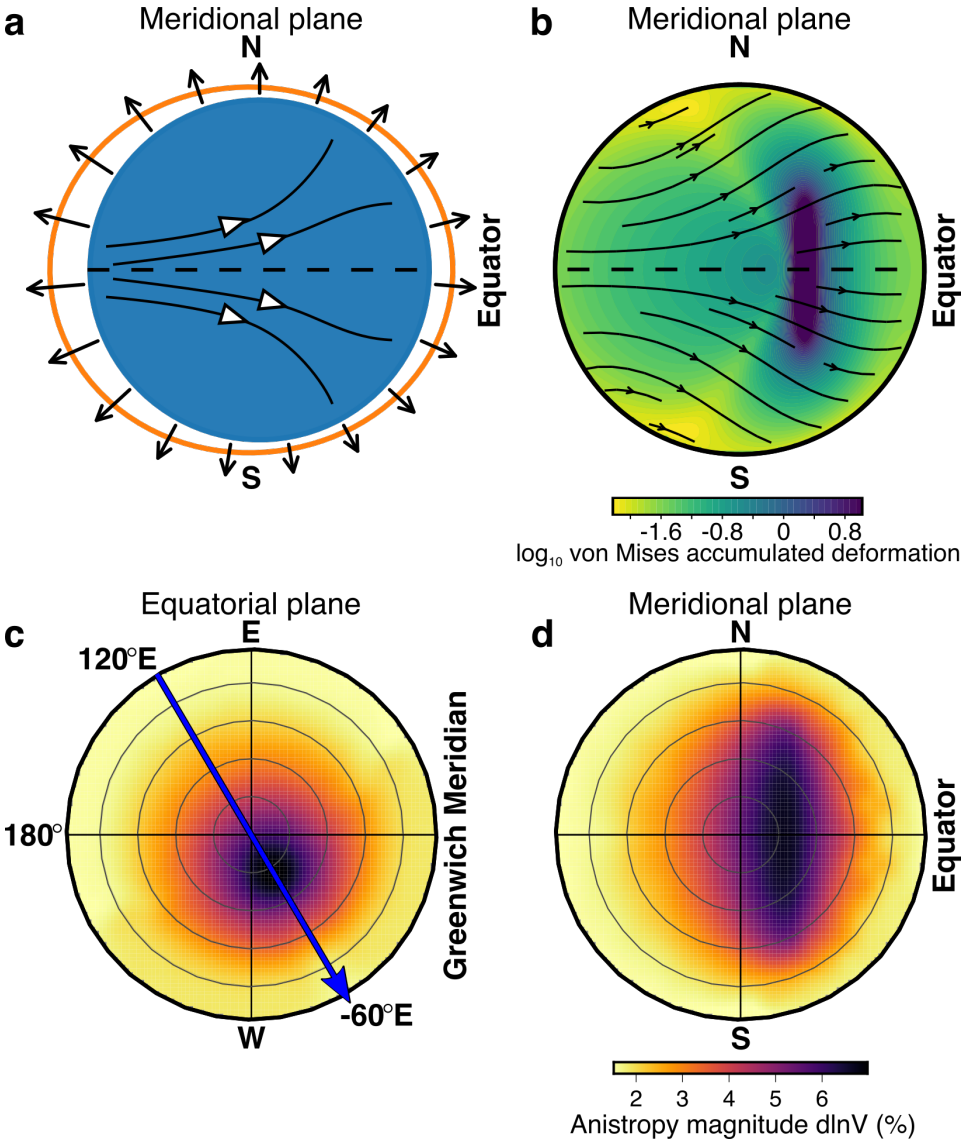

Fig. 3: Inner core growth, strain and anisotropy. (a) Sketch combining preferential equatorial growth (driven by Taylor column convection in the outer core) and asymmetric growth rate, with imposed IC growth rate at the boundary and internal flow shown by black and white arrows, respectively. **(b)** Asymmetric growth and movement in from the equator and towards the poles causing lateral and vertical advection of the strongest deformation. Both **(a)** and **(b)** show the meridional plane along the axis of translation with dashed line showing the equator. The strain field aligns iron grains, producing strong anisotropy in the deep IC that is offset from the rotation (N-S) axis in **(c)** the equatorial plane, and elongated parallel to the rotation axis in **(d)** the meridional plane along the direction of translation shown by the arrow in **(c)**. Calculated with IC age of 0.5 Ga, S2 of 0.6, translation rate of 0.3, and translation direction from 120°E to -60°W.

In our model, the present-day IC seismic anisotropy is a function of the initial single crystal anisotropy, the slip planes of crystal deformation, and the flow field. Crystallographic alignment of a polycrystal is necessary to generate significant anisotropy on the length scale

of the IC. Using Visco-Plastic Self-Consistent modelling (VPSC)[17] we calculate the anisotropy resulting from dislocation creep in the strain field produced by our geodynamic models, for different IC ages, translation rates, and single crystal structures. Despite body-centred cubic (bcc) iron having strong single crystal anisotropy[18], we find that it cannot produce strong polycrystal anisotropy, nor can face-centered cubic iron, as also previously shown[19]. In contrast, plastic deformation of a hexagonally close packed (hcp) iron-nickel alloy ($Fe_{93.75}Ni_{6.25}$[20]), compatible with cosmo-chemical constraints[21], with slip on the <c+a> pyramidal planes[22,23] produces an anisotropic IC with up to 6.6% anisotropy (Fig. 3d) that can fit the seismic data well. In this model, the fast direction of anisotropy becomes aligned with the rotation axis and the slow direction varies with depth (Extended Data Fig. 7), matching observations[24]. Pure hcp iron does not produce as strong a match to our observations (Extended Data Figs. 8 and 9).

The pattern and strength of the flow field induced by IC growth impacts the strain that crystals experience, and is controlled by the IC age, S2, translation rate, and the direction of translation. The IC age trades off linearly with strain rate and duration, but the dislocation creep has a non-linear relation between stress and strain rate (see Methods), implying that the degree and pattern of crystal alignment - and therefore the pattern and strength of the resulting seismic anisotropy varies with duration, and so IC age. The total strain is controlled by the parameter S2; thus, the strain rate is controlled by both IC age and S2. We constrain the IC growth history by running models with a range of ages, translation rates, and values of S2 and compare predicted anisotropy from these models with our seismic observations (Figure 4). The data is best fit by models with $0.4 \leq S2 \leq 0.8$. Within the range of acceptable IC ages[23-25] (see Methods), we find S2=0.6 and IC age of 0.5 Ga to best fit both the seismic observations and geodynamic constraints, although the constraint on age is not strong (Fig. 4d-f; See Methods). Translation at a rate of 0.3 IC radii over the 0.5 Ga IC lifetime along an axis oriented in the equatorial plane from 120°E towards -60°W matches the geographic pattern of anisotropy, achieving a 93% variance reduction for the polar data compared with 89% for a model with no translation. Our model shows increasing anisotropy strength with depth. The model also displays weak anisotropy near the ICB that is stronger in the WH than the EH, which is qualitatively compatible with models of hemispherically distinct isotropy in the upper IC from measurements of PKiKP[25] and P′P′df[26] travel times, and with constraints on the magnitude and distribution of anisotropy from normal modes[27,28].

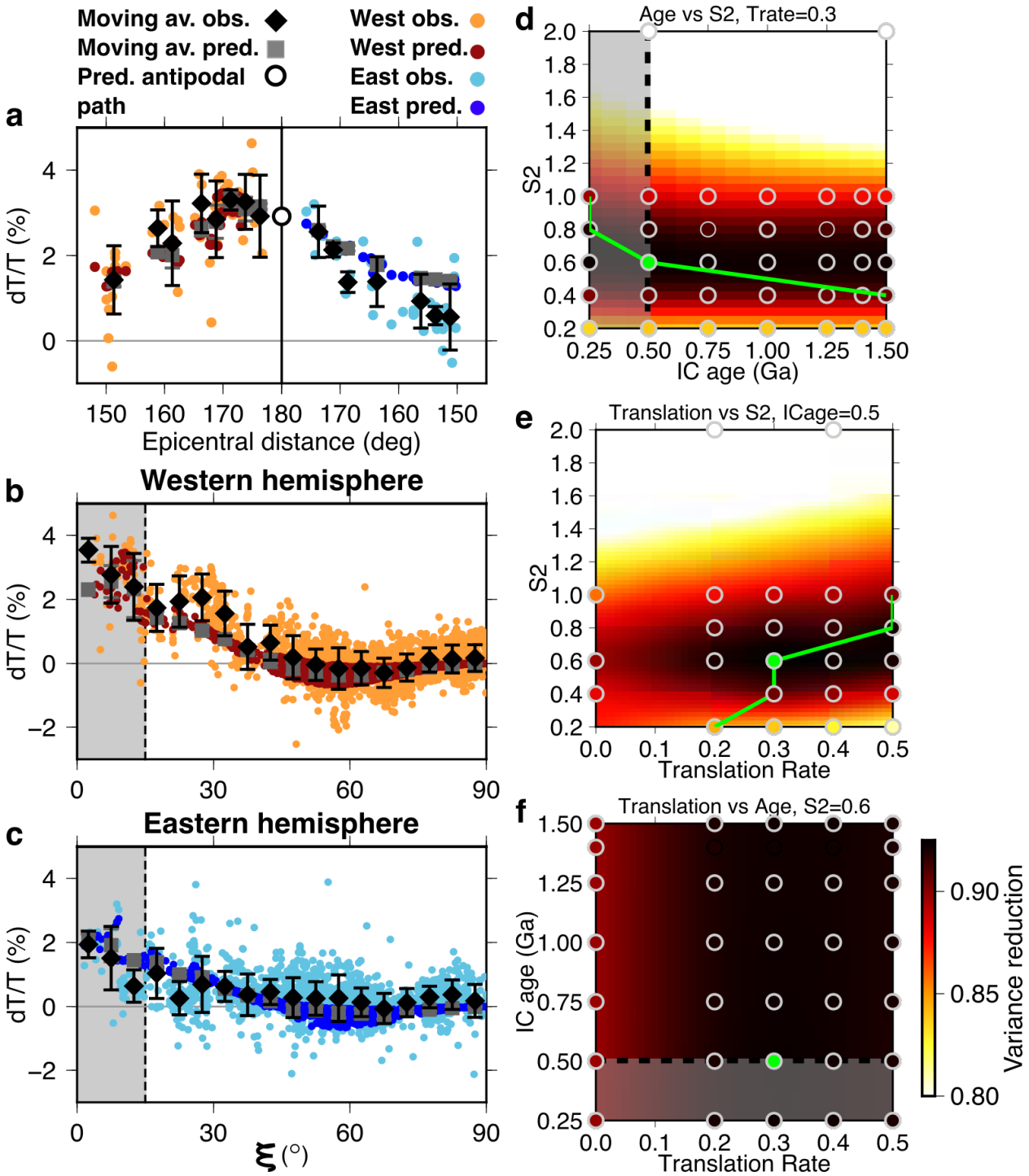

Fig. 4: Predicted versus observed PKP velocity anomalies for hcp Fe93.75Ni6.25 at 5500 K and 360 GPa[20] and trade-offs between IC age, S2, and translation rate. (a-c): Predicted (dark blue and red dots and with mean as grey squares) and observed (light blue and orange dots and with mean as black diamonds) effective velocity anomalies as a function of **(a)** epicentral distance for data with ξ≤15°, marked by shaded region in **(b)** and **(c)**, and as a function of ξ in the **(b)** western and **(c)** eastern hemispheres for IC growth model in Fig. 3. The open circle in **(a)** marks the predicted effective velocity anomaly for a path along the

rotation axis. Error bars for the data show the mean and one standard deviation at 2.5° and 5° increments for panels **(a),** and **(b)** and **(c)**, respectively. (**d-f**): Variance reduction of the model relative to the data illustrating the trade-offs between **(d)** IC age and S2, **(e)** S2 and translation rate, and **(f)** translation rate and IC age. Grey circles mark tested values, and the green circle marks the best-fitting parameters, corresponding to the model in **(a-c)** and at which the 3D space is sampled. The green line tracks the best x-value at any given y-value. Models in the shaded region have too young IC ages based on core conductivity. Surface is interpolated with a "minimum curvature" spline.

Remaining discrepancies between observations and predictions may result from contamination of the observations by mantle structure and small-scale structure in the IC. While differential measurements remove some of the effect of upper mantle heterogeneity on the PKP travel times, even modest 3D velocity structure deeper in the mantle can influence them[29]. The largest travel time anomalies that we observe (9.9 s) are for PKPab-df measurements between 170° and 175° distance, where there is large lateral separation between the two ray paths such that they could experience significantly different velocities in the deep mantle. Still, mantle velocity anomalies such as Ultra Low Velocity Zones (ULVZ) and the Large Low Shear Velocity Provinces (LLSVPs) could generate at most 1-2s travel time delays. Furthermore, the data with large travel time anomalies pierce the core-mantle boundary at distinctly different locations (Fig. 1b,c,d), and no ULVZs have yet been reported in these regions[30]. Thus, mantle structure would mostly introduce scatter and not significantly obscure the first-order IC anisotropic pattern that we model.

Implications for core and mantle evolution

Within the limits of the assumptions made, particularly the assumption of dislocation creep, the proposed model has implications for the physical properties of the IC. Assuming Yoshida-style deformation restricts the range of possible IC viscosities ($\eta > 10^{18}$ Pas), and the IC age to be larger than the diffusive time scale, which may range from 0.2 to 1.5 Ga[4], depending on the chosen core conductivity. This constraint places the viscosity at the upper end of the range recently obtained by density function theory[31].

Our model suggests that the seismic structure of the IC records the large-scale pattern of the heat flux at the ICB, which is controlled by the dynamics of the outer core and the heat flux variations at the CMB[12]. Our preferred model has a translation rate of 0.3 and a ratio of polar to equatorial growth (S2) of 0.6. This corresponds to a growth rate that is 40% lower at the poles and 130% larger at the equator compared to the global average. Growth rate at the equator varies between the eastern and western hemispheres from 100% to 160% of the global average rate, respectively. This pattern is similar to that obtained when forcing the geodynamo with heat fluxes at the top of the core based on present-day lower mantle structure[12] and suggests that the asymmetry in heat extraction has been stable in the outer core for times similar to the age of the IC. This agrees with indications that the currently observed LLSVPs separated by a ring of high seismic velocities at the base of the mantle may have been stable for at least 200-300 Ma[32–34], and with the potential existence of structures in the mantle stabilizing the convection pattern[35]. In contrast, geomagnetic observations of outer core patterns that imply forcing by bottom-up interactions[36] may indicate either a recent change in IC dynamics from passive to active dynamics or complex interactions

between the inner and outer core that may be described at smaller scales than are considered here. Our modeling supports a relatively high core conductivity, as it favors a young IC age (~0.5 Ga) and requires the absence of convective instabilities. Preventing the development of thermal instabilities with an IC age of 0.5 Ga requires IC thermal conductivity >120 W/m/K[4]. Better resolving 3D patterns of seismic anisotropy in the IC may help document further the uneven growth history of the IC, providing a record of the global scale pattern of outer core dynamics. While our model does not consider the smaller-scale seismic structure of the inner core[37], we provide the first holistic model of IC growth capable of matching the observed seismic anisotropy and consistent with available paleomagnetic observations and mineral physics data[38,39].

References

Poupinet, G., Pillet, R. & Souriau, A. Possible heterogeneity of the Earth's core deduced from PKIKP travel times. *Nature* **305**, 294–206 (1983).

2. Morelli, A., Dziewonski, A. M. & Woodhouse, J. H. Anisotropy of the inner core inferred from PKIKP travel times. *Geophys. Res. Lett.* **13**, 1545–1548 (1986).
3. Woodhouse, J. H., Giardini, D. & Li, X. -D. Evidence for inner core anisotropy from free oscillations. *Geophys. Res. Lett.* **13**, 1549–1552 (1986).
4. Lasbleis, M. & Deguen, R. Building a regime diagram for the Earth's inner core. *Phys. Earth planet. Int.* **247**, 80–93 (2015).
5. Lincot, A., Cardin, P., Deguen, R. & Merkel, S. Multiscale model of global inner-core anisotropy induced by hcp alloy plasticity. *Geophys. Res. Lett.* **43**, 1084–1091 (2016).
6. Tanaka, S. & Hamaguchi, H. Degree one heterogeneity and hemispherical variation of anisotropy in the inner core from *PKP* (BC)- *PKP* (DF) times. *J. Geophys. Res.* **102**, 2925–2938 (1997).
7. Creager, K. C. Large-scale variations in inner core anisotropy. *J. Geophys. Res.* **104**, 23127–23139 (1999).
8. Irving, J. C. E. & Deuss, A. Hemispherical structure in inner core velocity anisotropy. *J. Geophys. Res.* **116**, 1–17 (2011).
9. Lythgoe, K. H., Deuss, A., Rudge, J. F. & Neufeld, J. A. Earth's inner core: Innermost inner core or hemispherical variations? *Earth Planet. Sci. Lett.* **385**, 181–189 (2014).
10. Irving, J. C. E. Imaging the inner core under Africa and Europe. *Phys. Earth planet. Int.* **254**, 12–24 (2016).
11. Yoshida, S., Sumita, I. & Kumazawa, M. Growth model of the inner core coupled with the outer core dynamics and the resulting elastic anisotropy. *J. Geophys. Res.* **101**, 28085–28103 (1996).
12. Aubert, J., Amit, H., Hulot, G. & Olson, P. Thermochemical flows couple the Earth's inner core growth to mantle heterogeneity. *Nature* **454**, 758–761 (2008).
13. Deguen, R., Cardin, P., Merkel, S. & Lebensohn, R. A. Texturing in Earth's inner core due to preferential growth in its equatorial belt. *Phys. Earth planet. Int.* **188**, 173–184 (2011).
14. Deguen, R., Alboussière, T. & Labrosse, S. Double-diffusive translation of Earth's inner core. *Geophys. J. Int.* **214**, 88–107 (2018).
15. Alboussiëre, T., Deguen, R. & Melzani, M. Melting-induced stratification above the Earth's inner core due to convective translation. *Nature* **466**, 744–747 (2010).
16. Monnereau, M., Calvet, M., Margerin, L. & Souriau, A. Lopsided growth of Earth's

inner core. *Science (80-.).* **328**, 1014–1017 (2010).
17. Lebensohn, R. A. & Tomé, C. N. A self-consistent anisotropic approach for the simulation of plastic deformation and texture development of polycrystals: Application to zirconium alloys. *Acta Met. Mater.* **41**, 2611–2624 (1993).
18. Belonoshko, A. B. *et al.* Origin of the low rigidity of the earth's inner core. *Science (80-.).* **316**, 1603–1605 (2007).
19. Lincot, A., Merkel, S. & Cardin, P. Is inner core seismic anisotropy a marker for plastic flow of cubic iron? *Geophys. Res. Lett.* **42**, 1326–1333 (2015).
20. Martorell, B., Brodholt, J., Wood, I. G. & Vočadlo, L. The effect of nickel on the properties of iron at the conditions of Earth's inner core: Ab initio calculations of seismic wave velocities of Fe-Ni alloys. *Earth Planet. Sci. Lett.* **365**, 143–151 (2013).
21. McDonough, W. F. & Sun, S. s. The composition of the Earth. *Chem. Geol.* **120**, 223–253 (1995).
22. Miyagi, L. *et al.* In situ phase transformation and deformation of iron at high pressure and temperature. *J. Appl. Phys.* **104**, (2008).
23. Merkel, S., Gruson, M., Wang, Y., Nishiyama, N. & Tomé, C. N. Texture and elastic strains in hcp-iron plastically deformed up to 17.5GPa and 600K: Experiment and model. *Model. Simul. Mater. Sci. Eng.* **20**, (2012).
24. Frost, D. A. & Romanowicz, B. On the orientation of the fast and slow directions of anisotropy in the deep inner core. *Phys. Earth Planet. Inter.* **286**, 101–110 (2019).
25. Garcia, R. & Souriau, A. Inner core anisotropy and heterogeneity level. *Geophys. Res. Lett.* **27**, 3121–3124 (2000).
26. Frost, D. A. & Romanowicz, B. Constraints on Inner Core Anisotropy Using Array Observations of P′P′. *Geophys. Res. Lett.* **44**, 10,878-10,886 (2017).
27. Romanowicz, B., Li, X. D. & Durek, J. Anisotropy in the inner core: Could it be due to low-order convection? *Science (80-.).* **274**, 963–966 (1996).
28. Irving, J. C. E. & Deuss, A. Stratified anisotropic structure at the top of Earth's inner core: A normal mode study. *Phys. Earth planet. Int.* **186**, 59–69 (2011).
29. Bréger, L., Romanowicz, B. & Rousset, S. New constraints on the structure of the inner core from P'P'. *Geophys. Res. Lett.* **27**, 2781–2784 (2000).
30. Yu, S. & Garnero, E. J. Ultralow Velocity Zone Locations: A Global Assessment. *Geochem. Geophys. Geosyst.* **19**, 396–414 (2018).
31. Ritterbex, S. & Tsuchiya, T. Viscosity of hcp iron at Earth's inner core conditions from density functional theory. *Sci. Rep.* **10**, 2–5 (2020).
32. Torsvik, T. H., Smethurst, M. A., Burke, K. & Steinberger, B. Large igneous provinces generated from the margins of the large low-velocity provinces in the deep mantle. *Geophys. J. Int.* **167**, 1447–1460 (2006).
33. Dziewonski, A. M., Lekic, V. & Romanowicz, B. A. Mantle Anchor Structure: An argument for bottom up tectonics. *Earth Planet. Sci. Lett.* **299**, 69–79 (2010).
34. Greff-Lefftz, M. & Besse, J. Paleo movement of continents since 300Ma, mantle dynamics and large wander of the rotational pole. *Earth Planet. Sci. Lett.* **345–348**, 151–158 (2012).
35. Ballmer, M. D., Houser, C., Hernlund, J. W., Wentzcovitch, R. M. & Hirose, K. Persistence of strong silica-enriched domains in the Earth's lower mantle. *Nat. Geosci.* **10**, 236–240 (2017).
36. Aubert, J., Finlay, C. C. & Fournier, A. Bottom-up control of geomagnetic secular

variation by the Earth's inner core. *Nature* **502**, 219–223 (2013).
37. Tkalčić, H. Large variations in travel times of mantle-sensitive seismic waves from the South Sandwich Islands: Is the Earth's inner core a conglomerate of anisotropic domains? *Geophys. Res. Lett.* **37**, 1–6 (2010).
38. Biggin, A. J. *et al.* Palaeomagnetic field intensity variations suggest Mesoproterozoic inner-core nucleation. *Nature* **526**, 245–248 (2015).
39. Bono, R. K., Tarduno, J. A., Nimmo, F. & Cottrell, R. D. Young inner core inferred from Ediacaran ultra-low geomagnetic field intensity. *Nat. Geosci.* **12**, 143–147 (2019).

Corresponding author

For correspondence and requests for material please contact Daniel A Frost at dafrost@berkeley.edu.

Acknowledgements

The authors acknowledge the following funding sources: NSF grants EAR-1135452 and EAR-1829283 to DAF and BR; European Union's Horizon 2020 research and innovation program under the Marie Skłodowska-Curie Grant Agreement No. 795289 to ML; and NSF grant EAR 1343908 and DOE grant DE-FG02-05ER15637 to BC.

Author contributions

All authors contributed to project design, methodology development, model conceptualization and manuscript preparation. DAF was responsible for seismic data curation and formal analysis and wrote the first draft of the paper. ML contributed to the geodynamic modeling and BC provided the mineral physics input. DAF and BR coordinated the project.

Competing interests

No authors have any known competing interests.

Figure Legends

Fig. 1: Sampling of the inner core with polar PKP rays. (a) Ray paths of PKP branches used here. PKPdf samples the IC, while PKPbc and PKPab remain in the outer core. ξ is the angle that the PKPdf path in the IC makes with Earth's rotation axis. (b-d): Only polar paths (ξ<35°) from source to receiver colour-coded by effective IC velocity anomaly (line colour) and ξ (symbol colour) for paths turning between (b) 5200 and 5600 km depth, (c) 5600 km and 6000 km, and (d) 6000 km and Earth's centre. 530 polar paths are shown. Turning points for PKPbc-df and PKPab-df ray pairs are shown as diamonds and circles, respectively. We exclude the South Sandwich Islands (SSI) to Alaska paths. Grey region marks best fitting WH boundaries determined in this study and solid line marks the EH boundary[10].

Fig. 2: Effective velocity anomaly in the inner core from PKPab-df and PKPbc-df travel time observations as a function of ξ and epicentral distance. (a) Effective velocity anomalies as a function of ξ display a hemispherical pattern implying stronger anisotropy in the WH (red) than in the EH (blue). Data from the SSI to Alaska are excluded (Extended Data Figure 3). **(b)** IC velocity anomaly as a function of epicentral distance, and thus bottoming

radius of the ray in the WH (left) and EH (right), for data with ξ≤15° (shaded region in (**a**)). Solid lines mark linear fits as a function of distance in the respective hemispheres with mirror images across the centre of the Earth (180°) shown as broken lines. Moving averages (diamonds) and standard deviations at 2.5° increments in distance highlight the robust trends. The EH trend is extended to meet the WH trend (at 400 km radius) with a dotted blue line.

Fig. 3: Inner core growth, strain and anisotropy. (a) Sketch combining preferential equatorial growth (driven by Taylor column convection in the outer core) and asymmetric growth rate, with imposed IC growth rate at the boundary and internal flow shown by black and white arrows, respectively. **(b)** Asymmetric growth and movement in from the equator and towards the poles causing lateral and vertical advection of the strongest deformation. Both **(a)** and **(b)** show the meridional plane along the axis of translation with dashed line showing the equator. The strain field aligns iron grains, producing strong anisotropy in the deep IC that is offset from the rotation (N-S) axis in **(c)** the equatorial plane, and elongated parallel to the rotation axis in **(d)** the meridional plane along the direction of translation shown by the arrow in **(c)**. Calculated with IC age of 0.5 Ga, S2 of 0.6, translation rate of 0.3, and translation direction from 120°E to -60°W.

Fig. 4: Predicted versus observed PKP velocity anomalies for hcp Fe93.75Ni6.25 at 5500 K and 360 GPa[20] and trade-offs between IC age, S2, and translation rate. (a-c): Predicted (dark blue and red dots and with mean as grey squares) and observed (light blue and orange dots and with mean as black diamonds) effective velocity anomalies as a function of **(a)** epicentral distance for data with ξ≤15°, marked by shaded region in **(b)** and **(c)**, and as a function of ξ in the **(b)** western and **(c)** eastern hemispheres for IC growth model in Fig. 3. The open circle in **(a)** marks the predicted effective velocity anomaly for a path along the rotation axis. Error bars for the data show the mean and one standard deviation at 2.5° and 5° increments for panels **(a),** and **(b)** and **(c)**, respectively. (**d-f**): Variance reduction of the model relative to the data illustrating the trade-offs between **(d)** IC age and S2, **(e)** S2 and translation rate, and **(f)** translation rate and IC age. Grey circles mark tested values, and the green circle marks the best-fitting parameters, corresponding to the model in **(a-c)** and at which the 3D space is sampled. The green line tracks the best x-value at any given y-value. Models in the shaded region have too young IC ages based on core conductivity. Surface is interpolated with a "minimum curvature" spline.

Methods for: Seismic evidence of slow translation and preferential equatorial growth of the inner core

Authors: Daniel A. Frost[1]*, Barbara Romanowicz[123], Marine Lasbleis[45], Brian Chandler[1]

Seismology

We collect PKPab-df and PKPbc-df differential travel time measurements to determine inner core structure (Fig. 1). Differential travel time anomalies, calculated with respect to a 1D reference model, can thus be attributed to the IC, at least to first order.

Our dataset comprises the existing Berkeley (UCB) PKP travel time data collection[24,40–42] with additional data[43]. This collection includes 2944 and 1170 PKPab-df and PKPbc-df differential travel time measurements, respectively. Here, we have added a total of 614 PKPab-df and 416 PKPbc-df measurements from both recent events in the South Sandwich Islands between 23/10/2015 and 15/09/2017 observed in Alaska and other nearby stations in the northern hemisphere, and from events of m>5.5 at latitudes greater than 50°N between 1/1/2008 and 31/06/2017 observed at distances beyond 150° and stations in the southern hemisphere, collected using the SOD mass-downloader tool and IRIS Wilber3 tool (289 observations from South Sandwich Islands to Alaska and 741 observations from other high latitude events observed in Antarctica). These events were recorded at networks: YT07, ZM07, 2C, AI, AU, ER, G, GE, II, IU, PS, SY, C, 9G, ID.

Locations and arrival times for events before and after 2009 are from the EHB[44] and ISC catalogues, respectively. We removed the linear trend and mean from vertical component data, deconvolved the instrument response to velocity. Data were bandpass filtered between 0.4-2.0 Hz, and the Hilbert transform was applied to take account of the phase shift between PKPab and PKPdf. We manually picked phase onsets relative to predicted times from the 1D reference model ak135[45] after applying ellipticity corrections[46]. PKPdf and PKPbc are picked on the untransformed data, while PKPab is picked on the Hilbert transformed data. We classified picks based on the clarity of the signal onset, and the prominence of the signal in the unfiltered trace. Following picking and classification, we retained 614 and 416 highest quality differential PKPab-df and PKPbc-df travel times, respectively, measured with respect to ak135 (all data are shown, split by quality, in Extended Data Fig. 2). These new measurements, combined with the existing catalogues mentioned above yield 3558 and 1586 high quality PKPab-df and PKPbc-df measurements, respectively. We only use the high-quality data for all plots and calculations in this paper.

Attributing the entire travel-time anomaly to structure in the IC, we convert travel times to velocity anomalies relative to 1D model ak135[45] as: $-\frac{dT}{Tic} = \frac{dv}{v}$, where Tic and v are reference travel times and velocities in the IC, respectively. This accounts for the difference in path length between the shallow and more deeply travelling waves. We construct cylindrically symmetric models of anisotropy, in which the perturbation to a spherically symmetric model[47] is expressed as:

$$\frac{\delta v}{v} = a + b\cos^2\xi + c\cos^4\xi \quad \text{(S1)}$$

where v and δv represent the reference velocity and velocity perturbations, respectively and ξ is the angle of the ray path direction at the bottoming point of the ray with respect to Earth's rotation axis. We determine the coefficients a, b, and c (which can depend on depth and location, depending on the model considered) by fitting our data with an L1-norm to account for outliers. The apparent IC velocity anomaly will be the integrated effect of the velocity anomalies along the raypath in the inner core.

In order to best illustrate the hemispherical differences, we update hemisphere boundaries by grid searching for the location of the western boundary of the western hemisphere. We hold the eastern boundary fixed to that previously found[10] as our dataset has limited coverage in this region, while the previous study was designed to sample the eastern boundary. Seeking to test the model of an IC with hemispherical and depth dependent anisotropy, we split the data into two hemispheres described by the candidate boundaries and fit models of velocity anomaly as a function of distance to the polar data ($\xi \leq 15°$). Only the polar data shows significant hemisphericity, thus we exclude higher ξ data to avoid biasing the fit with data with little resolving power. We seek to minimise the combined misfit to the two straight lines (Extended Data Fig. 6). Hemispheres are assigned based on the longitude of the turning point of the ray, an approximation that works well for polar data, but for equatorial data leads to smearing of hemispherical differences. However, since equatorial data do not show significant differences between hemispheres this approximation is not problematic. The western boundary of the western hemisphere produces equal fits to the data when located between -166° E and -159° E, with a very sharp falloff in R^2 at locations <-166° E or >-153° E. While we simplify the boundary to a line of constant longitude, we cannot rule out a bent western boundary[48]. When we repeat this test with the less-polar data, ξ<35°, the best fitting hemisphere locations are similar with a sharp falloff at <-153° E.

To determine the robustness of the resolved gradients of velocity with depth in each hemisphere we perform an interaction effect analysis using the data shown in Fig. 2b. We find that to 95% confidence we cannot reject the null hypothesis that the gradient of the two hemispheres is the same, i.e. the gradient of the two hemispheres is statistically the same. To determine the robustness of the offset in intercept between the two gradients we perform a bootstrap resampling of the same data. We find that the second standard deviations about the bootstrapped means do not overlap between the two hemispheres. We conclude that the trends of velocity with depth in the two hemispheres have statistically distinct intercepts but statistically very similar gradients.

South Sandwich Islands to Alaska anomaly

PKPbc-df and PKPab-df data recorded at stations in Alaska show a spread of travel time anomalies that do not match the global pattern as a function of ξ (Extended Data Fig. 3), as previously reported[37,49,50]. This is especially clear for PKPbc-df measurements that show travel time anomalies of up to 6 s, in contrast to measurements outside of Alaska of less than 3 s on the most polar paths. This data may be contaminated by the Alaska slab[49]. We thus

remove data recorded in Alaska from the analysis presented here, but we keep data from events in Alaska, which are not affected by the slab and fit the global trends (Extended Data Fig. 3).

Geodynamics

It has previously been proposed by different groups that viscous relaxation of topography at the inner core boundary, caused by differential growth rate of the inner core, may orientate crystals in the inner core and explain the inner core bulk anisotropy (Extended Data Fig. 10)[11]. Flows in the inner core induced by preferential growth at the equator have a vertical cylindrical axis of symmetry and tend to align the crystals along this axis close to the center of the inner core. However, such a model cannot explain the observation of hemispherical differences in IC anisotropy. Meanwhile, lateral translation caused by either simultaneous melting and crystallisation on opposite sides of the IC[15,16] or an unstable compositional gradient[12,14] has been proposed to explain the hemispherical dichotomy in the IC.

Here we consider the flows induced by differential growth rate at the inner core boundary, where the differential growth rate is a sum of two previously studied patterns: preferential equatorial growth and hemispherical asymmetric growth (Supplementary Information Fig. 1). We consider neutral density stratification of the inner core, as it is the only regime in which deformation occurs at depth[4]. This drastically reduces the parameter space where such a flow could be observed, as a slightly unstable density stratification develops large-scale convection[51] and a stable density stratification inhibits radial flows and layers of high deformation develop near the inner core boundary[13]. As discussed before[4], preferential growth at the equator would still develop large-scale flows for stable stratification for large viscosity values ($\eta > 10^{18}$ Pa.s) and an age of inner core larger than the diffusive time scale (0.2-1.5 Ga). The assumption of Yoshida-style convection thus restricts the range of possible viscosities for the IC.

We solve the conservation of momentum equation for an incompressible fluid of constant viscosity η and constant density ρ in a spherical shell whose radius is increases with time as $R_{ic}(t) = R_{ic}(\tau_{ic})\sqrt{t/\tau_{ic}}$ from time 0, representing the nucleation of the inner core, to time τ_{ic}, today. The assumption of neutral stratification allows for a complete analytical solution for the flow for both the equatorial[11] and hemispherical patterns.

To determine the trajectory of a particle in the inner core, we fix the position of the particle today (at τ_{ic}) and integrate the trajectory backward in time using GrowYourIC[52]. The intersection of the trajectory and the ICB in the past corresponds to the time of crystallisation of the material.

We output the positions, velocity components, and velocity gradients of the particles with time and use this to calculate crystal orientations. To obtain a first idea of the deformation experienced by the particle, we calculate the vonMises equivalent strain rate and its average over the trajectory for $t_{\text{crystallisation}} > 0$.

In modelling the growth and resulting strain in the inner core, we also test the dependence of S2 on the preferred IC age and translation rate. We explore translation rates between 0

and 0.5 in increment of 0.1 radii of the IC over the age of the IC, IC ages between 0.25 and 1.5 in increments of 0.25, and S2 between 0.2 and 1.0 in increments of 0.2, searching for the model that best matches the observed anisotropy. Such slow translation rates, which are lower than the crystallisation rate, require only differential freezing and no melting, unlike models of fast translation[15,16]. We calculate the core growth and translation for non-dimensionalised time and IC size. We then scale the model using the radius of the inner core at the present day (1217.5 km) and the chosen age of the inner core. Thus, we scale the instantaneous strain rate by the inverse of the IC age ($1/\tau_{ic}$) and the time step (dt) by the IC age ($dt * \tau_{ic}$). Inner core age linearly affects the strain rate, but the maximum total accumulated strain for all IC ages is equal to S2, thus the value of S2 affects the total accumulated strain and the strain rate, while IC age only affects the strain rate. For each inner core age, S2, and translation rate, we use VPSC to calculate the resulting deformation. We model deformation by dislocation-creep, thus strain-rate and time step have a non-linear influence on the generation of anisotropy. Comparison of the resultant anisotropy models with our seismic observations suggest best-fitting ages between 0.5 and 1.5 Ga, depending on S2, with a translation rate of 0.3 radii over the age of the IC. Since models with S2<0.4 generate too little anisotropy to match the data and models with S2≥0.8 require an IC age of 0.25 Ga (which is likely too young[53–55]), we determine reasonable bounds for S2 of 0.4≤S2≤0.6, with the age trading off accordingly between 1.5 and 0.5 Ga, respectively. External constraints on the parameter S2 are poor, but previous work based on outer core geodynamics considerations[12] has preferred S2=0.4, which is consistent with our preferred range. The data can be fit by models with ages that are consistent with the range suggested from paleomagnetic constraints (between 0.5 Ga and 1.3 Ga[38,39]).

Anisotropy strength depends on IC age and S2 thus by matching the observed strength of anisotropy for a given S2 we can estimate IC age. Models with S2=0.4 and inner core ages >0.5 Ga generate strong and localised anisotropy capable of matching our observations. Models run with inner core ages <0.5 Ga have maximum anisotropies of less than 6.0%, and the volume of the IC with maximum anisotropy is very small. These models predict weaker anisotropy and lower gradients of anisotropy with depth than what we observe. In contrast, for older inner cores the maximum anisotropy reaches ~7.0% in places, thus achieves nearly full alignment of crystals, for which anisotropy would be 7.5%. For S2=0.6 inner core ages ≥0.5 predict strong anisotropy with a maximum anisotropy of ~7.0% in places, equivalent to the models with S2=0.4 and IC age ≥1.0 Ga. In fact, for S2=0.6 and IC ages >1.0 Ga, the models begin to predict anisotropy that is stronger than the observations. Age of the IC also depends on IC viscosity through its influence on strain rate, but the viscosity is fixed to $>10^{18}$ Pa-s by our assumption of Yoshida-style deformation[4]. Alternative solutions to fit the large anisotropy would be either easier deformation of hcp iron-nickel alloy than in our VPSC simulation, stronger single crystal anisotropy, or pressure dependence of the single crystal anisotropy (Extended Data Figure 9). However, both the deformation behaviour and precise anisotropic pattern of iron and iron alloys at high pressures and temperatures are not well constrained.

We rotate the resulting model of anisotropy about the rotation axis and in the equatorial plane through 360° in 10° increments and compare the misfit with the data. We thus find that the best fitting growth direction is from 120°E towards 60°W, placing the points of

fastest and slowest growth under the Banda Sea and Brazil, respectively. Interestingly, these are very similar to the foci of growth and melting modelled by [16], albeit with the opposite direction of growth.

Mineral physics

We calculate the anisotropy that would result from a deformation of an IC of a given composition in the presence of the strain field described above. An important component is the composition chosen, as anisotropy of the single crystal controls the anisotropy of the bulk model after deformation. Experimental studies indicate that hexagonally close packed (hcp) iron is stable at IC conditions[56], but this is complicated by the presence of lighter elements in the IC. The body centred cubic (bcc) iron phase may also be stable[57], depending on the strain field[58]. First principles calculations estimate the anisotropy of pure single iron crystals to range from 4.9-7.9% for hcp iron (given as the total range from minimum to maximum *dlnV*), and up to 14.7% for bcc iron[18,42,59], and potentially up to 20% near the melting point of hcp iron[60], although there is debate over the trends of anisotropy as a function of pressure and temperature[59,61–64]. The pattern of anisotropy for iron near its melting point[60] is very different from the observed IC anisotropy. Alloys of iron with plausible light elements modify the character of anisotropy, but the limited number of experiments leaves the dependence on pressure and temperature uncertain[20,65–69]. We select hcp iron-nickel alloy ($Fe_{93.75}Ni_{6.25}$[20]) as its pattern of single crystal anisotropy (Supplementary Information Fig. 11) is most similar to the observed anisotropy (Extended Data Figs. 3 and 4) and it is consistent with cosmo-chemical calculations of the core's composition[21].

We calculate the development of Crystal Preferred Orientation (CPO) in the presence of the strain field resulting from our above inner core growth models using the Visco-Plastic Self-Consistent modelling code (VPSC)[17]. Groups of 1500 particles, representing crystals of hcp iron-nickel alloy ($Fe_{93.75}Ni_{6.25}$) are generated at the Inner Core Boundary throughout the growth history of the inner core. Crystal growth at the ICB may cause pre-texuring[70]. We model particles with an initial solidification pre-texture in which the c-axes of the hcp iron crystals are oriented in the plane of the ICB, as in previous work[5]. The group of particles deforms as it is subject to the strain along the tracer path. The deformation is controlled by the crystal slip systems, for which we use those of hcp iron. Following from a previous study[5], we allow slip along the <c+a> pyramidal planes of hcp iron and lock the remaining slip systems and we set the normalized critically resolved shear stresses to ∞ for the basal <a>, prismatic <a>, and pyramidal <a> plane slip systems, and 0.5 for the pyramidal <c+a> plane slip system. We measure the resultant CPO at the present day.

CPO developed at each step of the growth model is combined with its respective elastic tensor to determine the resultant anisotropy. We incorporate estimates of the elastic tensors resulting from *ab initio* molecular dynamic simulations. For our chosen hcp FeNi alloy, elastic tensors are only available at 0 K and 360 GPa, and 5500 K and 360 GPa[20]. The temperature range of the inner core is likely very small – on the order of 30 K[71]. We thus neglect the pressure and temperature dependence of the elastic constants and calculate the resultant CPO for $Fe_{93.75}Ni_{6.25}$ alloy at 5500 K and 360 GPa (Supplementary Information Fig. 11). The discrepancy between the observed and predicted anisotropy in the eastern

hemisphere (Figure 4a) may result from the single crystal anisotropy being fixed with respect to pressure, thus not allowing weak enough anisotropy to match the data.

We seek to understand the influence of the physical state with depth in the IC on the elastic tensors. As above, we neglect the temperature dependence given its small impact on elastic tensors but consider the influence of pressure. Given the limited data for FeNi alloys, we assess the effects of the pressure dependence of anisotropy using pure Fe, for which there are data at a range of pressures from *ab initio* calculations[20,59]. Pressure as a function of radius was extracted from the Preliminary Reference Earth Model (PREM)[72] where the pressure ranges from 330 GPa at the inner core boundary (ICB) to 364 GPa at the centre of the Earth. A reference point of 360 GPa and 5500 K was chosen, and the derivatives of pressure at a constant temperature were determined by a middle difference method using results from the above-mentioned studies. Elastic constants from the reference point were then interpolated using a Taylor expansion to the 2nd derivative of pressure from the reference point to the pressure at each location along the geodynamic streamline (Extended Data Fig. 9). We find that at pressures of the ICB, pure hcp Fe would show weaker anisotropy of 5% and stronger anisotropy of 7% at the centre of the IC.

To predict travel time anomalies generated by the modelled anisotropy, we trace rays through 1D velocity model ak135 between the ICB piercing points for each of our observations using TauP[73], assuming propagation along the theoretical raypath in the 1D model. We interpolate the anisotropy model to a 50×50×50 km grid spacing and interpolate the ray to increase spatial sampling. For each ray segment, we find the anisotropy at the nearest model location, measure the ξ angle of the ray segment, calculate the velocity anomaly for that ξ angle using Christoffel's equation, and calculate the resulting travel time anomaly given the length of the ray segment. We sum the travel time anomalies over the ray to find the total predicted anomaly for each path through the anisotropy model. We calculate the variance reduction between the observed and predicted travel time anomalies for the most polar data, ξ<15°, without separating hemispheres.

References

40. Tkalčić, H., Romanowicz, B. & Houy, N. Constraints on D′′ structure using PKP (AB–DF), PKP (BC–DF) and PcP–P traveltime data from broad-band records. *Geophys. J. Int.* **148**, 599–616 (2002).
41. Cao, A. & Romanowicz, B. Test of the innermost inner core models using broadband PKIKP travel time residuals. *Geophys. Res. Lett.* **34**, 1–5 (2007).
42. Romanowicz, B. *et al.* Seismic anisotropy in the Earth's innermost inner core: testing structural models against mineral physics predictions. *Geophys. Res. Lett.* 93–100 (2015). doi:10.1002/2015GL066734
43. Tkalčić, H., Young, M., Muir, J. B., Davies, D. R. & Mattesini, M. Strong, Multi-Scale Heterogeneity in Earth's Lowermost Mantle. *Sci. Rep.* **5**, 1–8 (2015).
44. Robert Engdahl, E., Van Hilst, R. Der & Buland, R. Global teleseismic earthquake relocation with improved travel times and procedures for depth determination. *Bull. Seismol. Soc. Am.* **88**, 722–743 (1998).
45. Kennett, B. L. N., Engdahl, E. R. & Buland, R. Constraints on seismic velocities in the Earth from traveltimes. *Geophys. J. Int.* **122**, 108–124 (1995).

46. Kennett, B. L. N. & Gudmundsson, O. Ellipticity corrections for seismic phases. *Geophys. J. Int.* **127**, 40–48 (1996).
47. Creager, K. C. Anisotropy of the inner core from differential travel times of the phases\nPKP and PKIKP. *Nature* **356**, 309–314 (1992).
48. Yu, W. che *et al.* The inner core hemispheric boundary near 180 °W. *Phys. Earth planet. Int.* **272**, 1–16 (2017).
49. Romanowicz, B., Tkalčić, H. & Bréger, L. On the Origin of Complexity in PKP Travel Time Data. *Earth's Core Dyn. Struct. Rotat.* 31–44 (2003). doi:10.1029/GD031p0031
50. Romanowicz, B. & Wenk, H. R. Anisotropy in the deep Earth. *Phys. Earth planet. Int.* **269**, 58–90 (2017).
51. Deguen, R., Olson, P. & Reynolds, E. F-layer formation in the outer core with asymmetric inner core growth. *Comptes rendus - Geosci.* **346**, 101–109 (2014).
52. Lasbleis, M., Waszek, L. & Day, E. A. GrowYourIC: A Step Toward a Coherent Model of the Earth's Inner Core Seismic Structure. *Geochem. Geophys. Geosyst.* **18**, 4016–4026 (2017).
53. Pozzo, M., Davies, C., Gubbins, D. & Alfè, D. Thermal and electrical conductivity of iron at Earth's core conditions. *Nature* **485**, 355–358 (2012).
54. Dobson, D. Earth's core problem. *Nature* **534**, 45 (2016).
55. Ohta, K., Kuwayama, Y., Hirose, K., Shimizu, K. & Ohishi, Y. Experimental determination of the electrical resistivity of iron at Earth's core conditions. *Nature* **534**, 95–98 (2016).
56. Tateno, S., Hirose, K., Ohishi, Y. & Tatsumi, Y. The Structure of Iron in Earth's Inner Core. *Science (80-.).* **330**, 359–362 (2010).
57. Belonoshko, A. B. *et al.* Stabilization of body-centred cubic iron under inner-core conditions. *Nat. Geosci.* **10**, 312–316 (2017).
58. Vočadlo, L. *et al.* The stability of bcc-Fe at high pressures and temperatures with respect to tetragonal strain. *Phys. Earth planet. Int.* **170**, 52–59 (2008).
59. Vočadlo, L., Dobson, D. P. & Wood, I. G. Ab initio calculations of the elasticity of hcp-Fe as a function of temperature at inner-core pressure. *Earth Planet. Sci. Lett.* **288**, 534–538 (2009).
60. Martorell, B., Vocădlo, L., Brodholt, J. & Wood, I. G. Strong premelting effect in the elastic properties of hcp-Fe under inner-core conditions. *Science (80-.).* **342**, 466–468 (2013).
61. Steinle-Neumann, G., Stixrude, L., Cohen, R. E. & Gülseren, O. Elasticity of iron at the temperature of the Earth's inner core. *Nature* **413**, 57–60 (2001).
62. Gannarelli, C. M. S., Alfè, D. & Gillan, M. J. The particle-in-cell model for ab initio thermodynamics: Implications for the elastic anisotropy of the Earth's inner core. *Phys. Earth planet. Int.* **139**, 243–253 (2003).
63. Gannarelli, C. M. S., Alfè, D. & Gillan, M. J. The axial ratio of hcp iron at the conditions of the Earth's inner core. *Phys. Earth planet. Int.* **152**, 67–77 (2005).
64. Antonangeli, D., Merkel, S. & Farber, D. L. Elastic anisotropy in hcp metals at high pressure and the sound wave anisotropy of the Earth's inner core. *Geophys. Res. Lett.* **33**, 1–5 (2006).
65. Wu, X., Mookherjee, M., Gu, T. & Qin, S. Elasticity and anisotropy of iron-nickel phosphides at high pressures. *Geophys. Res. Lett.* **38**, 10–13 (2011).
66. Mookherjee, M. Elasticity and anisotropy of Fe 3 C at high pressures. *Am. Mineral.* **96**,

1530–1536 (2011).
67. Mookherjee, M. *et al.* High-pressure behavior of iron carbide (Fe 7 C 3) at inner core conditions. *Geophys. J. Int.* **116**, (2011).
68. Martorell, B., Wood, I. G., Brodholt, J. & Vočadlo, L. The elastic properties of hcp-Fe1 − xSixat Earth's inner-core conditions. *Earth Planet. Sci. Lett.* **451**, 89–96 (2016).
69. Li, Y., Vočadlo, L., Alfè, D. & Brodholt, J. Mg partitioning between solid and liquid iron under the Earth's core conditions. *Phys. Earth planet. Int.* **274**, 218–221 (2018).
70. Bergman, M. I. Measurements of electric anisotropy due to solidification texturing and the implications for the Earth's inner core. *Nature* **389**, 60–63 (1997).
71. Stacey, F. D. & Davis, P. M. High pressure equations of state with applications to the lower mantle and core. *Phys.* **142**, 137–184 (2004).
72. Dziewonski, A. M. & Anderson, D. L. Preliminary reference Earth model. *Phys.* **25**, 297–356 (1981).
73. Crotwell, H. P., Owens, T. J. & Ritsema, J. The TauP Toolkit: Flexible Seismic Travel-time and Ray-path Utilities. *Seismol. Res. Lett.* **70**, 154–160 (1999).
74. Waszek, L., Irving, J. & Deuss, A. Reconciling the hemispherical structure of Earth's inner core with its super-rotation. *Nat. Geosci.* **4**, 264–267 (2011).
75. Wessel, P., Luis, J. F., Uieda, L., Scharroo, R., Wobbe, F., Smith, W. H. F., & Tian, D. (2019). The Generic Mapping Tools version 6. *Geochemistry, Geophysics, Geosystems*, 20, 5556–5564. https://doi.org/10.1029/2019GC008515
76. MarineLasbleis/GrowYourIC: v0.6 (Version v0.6). Zenodo http://doi.org/10.5281/zenodo.4560747)

Data availability statement

The seismic travel time measurements that support the findings of this study (Figures 1, 2, 4, and Extended Data Figures 2, 3, 4, 6 and 8) are available in the supplements and at https://doi.org/10.5281/zenodo.4721364. Raw seismic waveform data and metadata are accessible through the facilities of IRIS Data Services, and specifically the IRIS Data Management Center. The EHB On-line Bulletins are available from the International Seismological Centre (ISC), for access to the EHB see https://doi.org/10.31905/PY08W6S3

Code availability statement

VPSC7 code is available on request from Dr. Ricardo A. Lebensohn. Information about accessing the code can be found at: https://public.lanl.gov/lebenso/
GrowYourIC code is available at https://github.com/MarineLasbleis/GrowYourIC and this work uses the v0.6 (Marine Lasbleis. (2021, February 24). MarineLasbleis/GrowYourIC: v0.6 (Version v0.6). Zenodo. http://doi.org/10.5281/zenodo.4560747)
Plots were produced using Generic Mapping Tools (Wessel et al., 2019; https://doi.org/10.1029/2019GC008515).

Extended Data

List of Extended Data figures:

Extended Data Figures 1-9

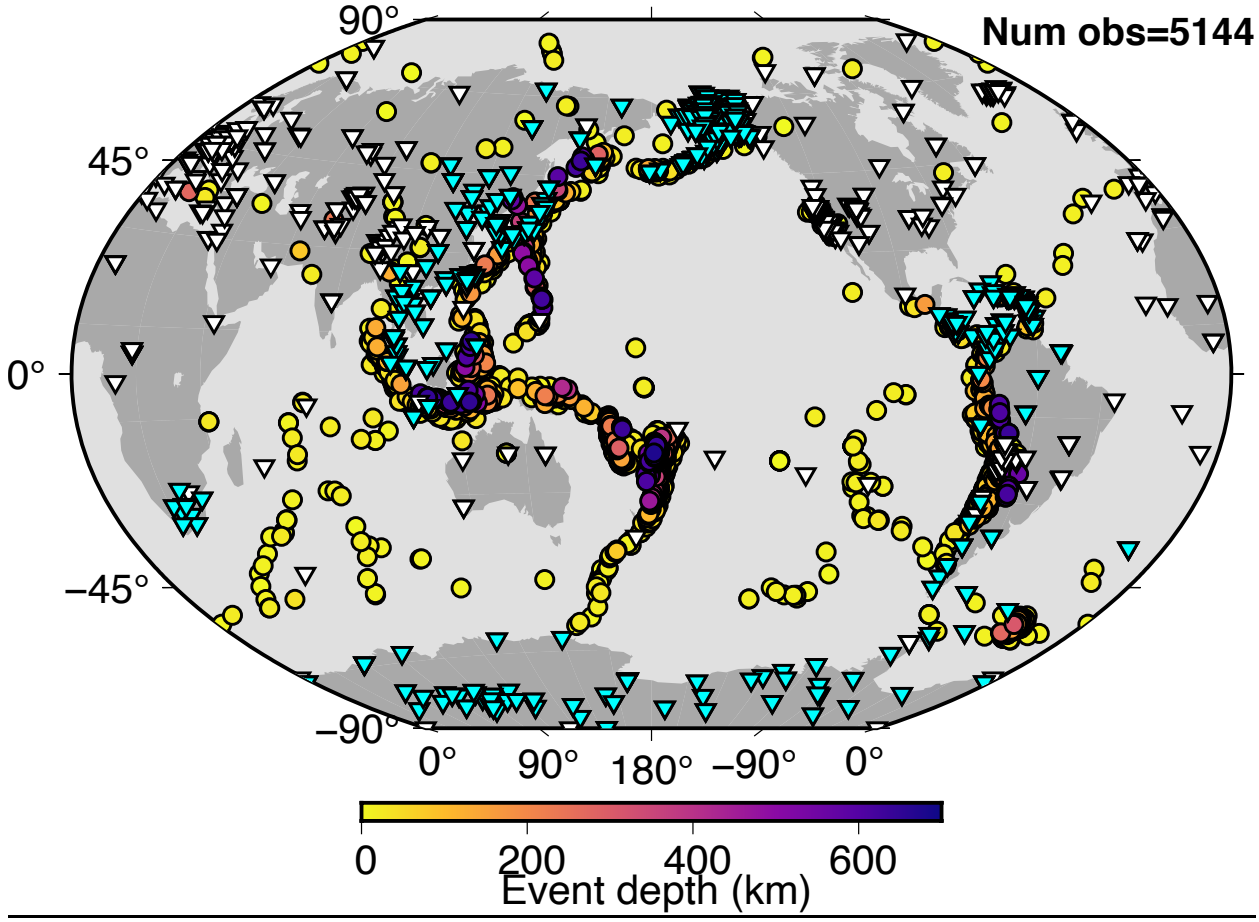

Extended Data Figure 1: Distribution of sources of receivers. Locations of sources (circles) and receivers (triangles) used in this study. Stations with newly acquired data are shown in cyan.

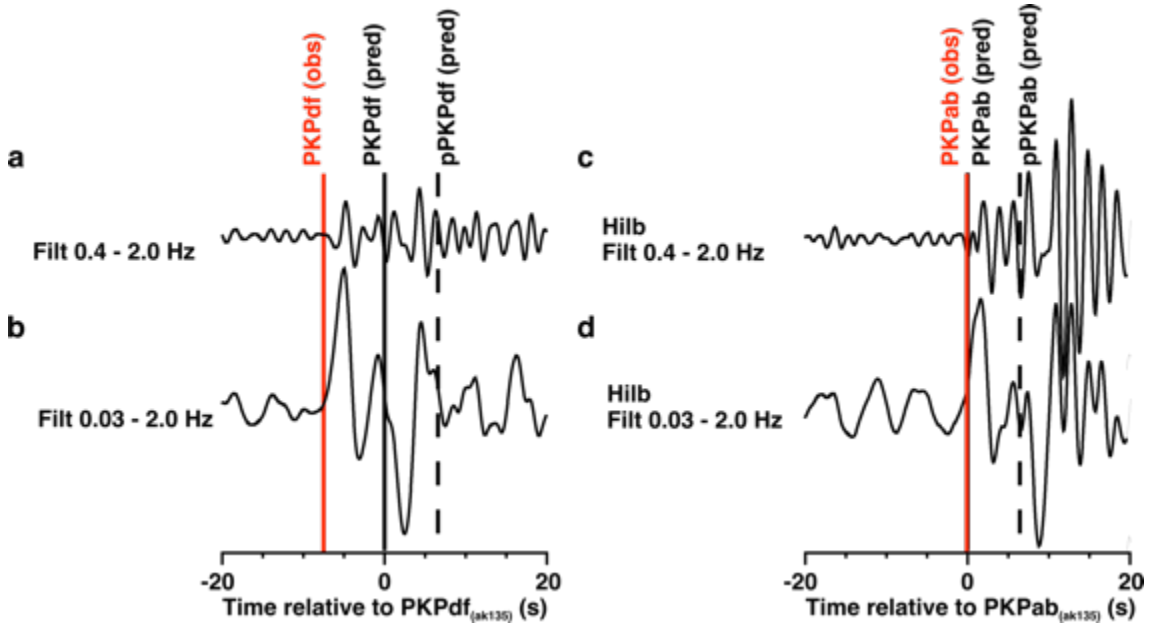

Extended Data Figure 2: Measuring PKP differential travel times. Example waveforms of (left) PKPdf and (right) PKPab for a M6.0 event in Baffin Bay on 2009/07/07 observed at station P124 in Antarctica. Waveforms are aligned on the predicted arrival time of the respective phases. Waveforms are shown as (a-c) broadly filtered at 0.03-2 Hz, (b-d) narrowly filtered at 0.4-2.0 Hz. In (c) and (d) waveforms have been Hilbert transformed. Measured arrival times are shown as red lines. Predicted arrivals (in model ak135 with ellipticity corrections) are shown by black solid and dashed lines for direct and depth phases, respectively.

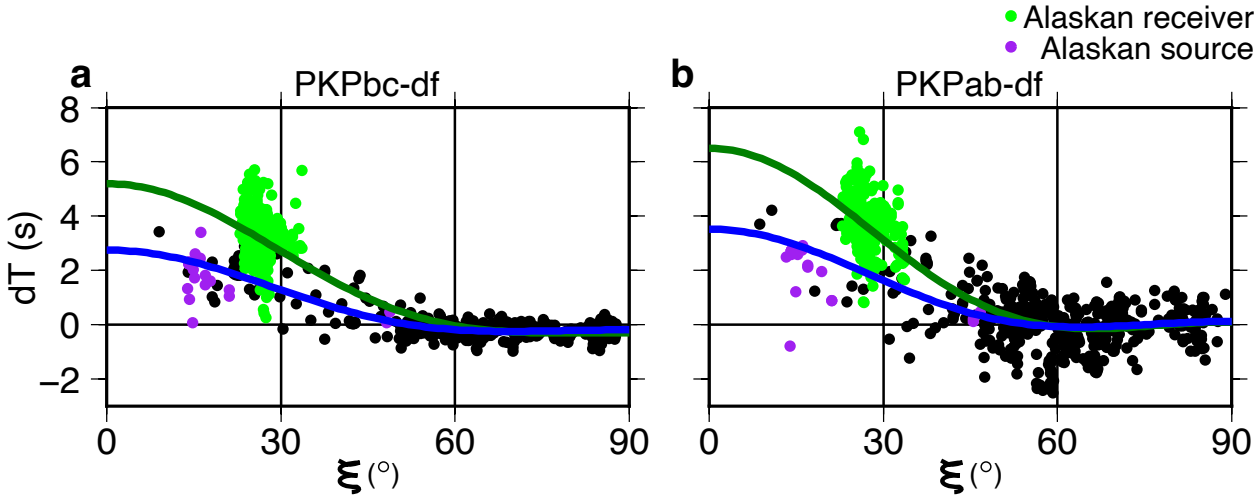

Extended Data Figure 3: Differential travel time anomalies for western hemisphere data turning within 450 km of the ICB with respect to model ak135, as a function of angle to the rotation axis, ξ. Travel time anomalies of **(a)** PKPbc-df and **(b)** PKPac-df phase pairs showing that observations at stations in Alaska (green) do not fit the global pattern, while observations from sources in Alaska (purple) do. Anisotropy curves are calculated using equation S1, assuming constant cylindrical anisotropy through the inner core, for all data (green curve) and all data except that recorded in Alaska (blue curve).

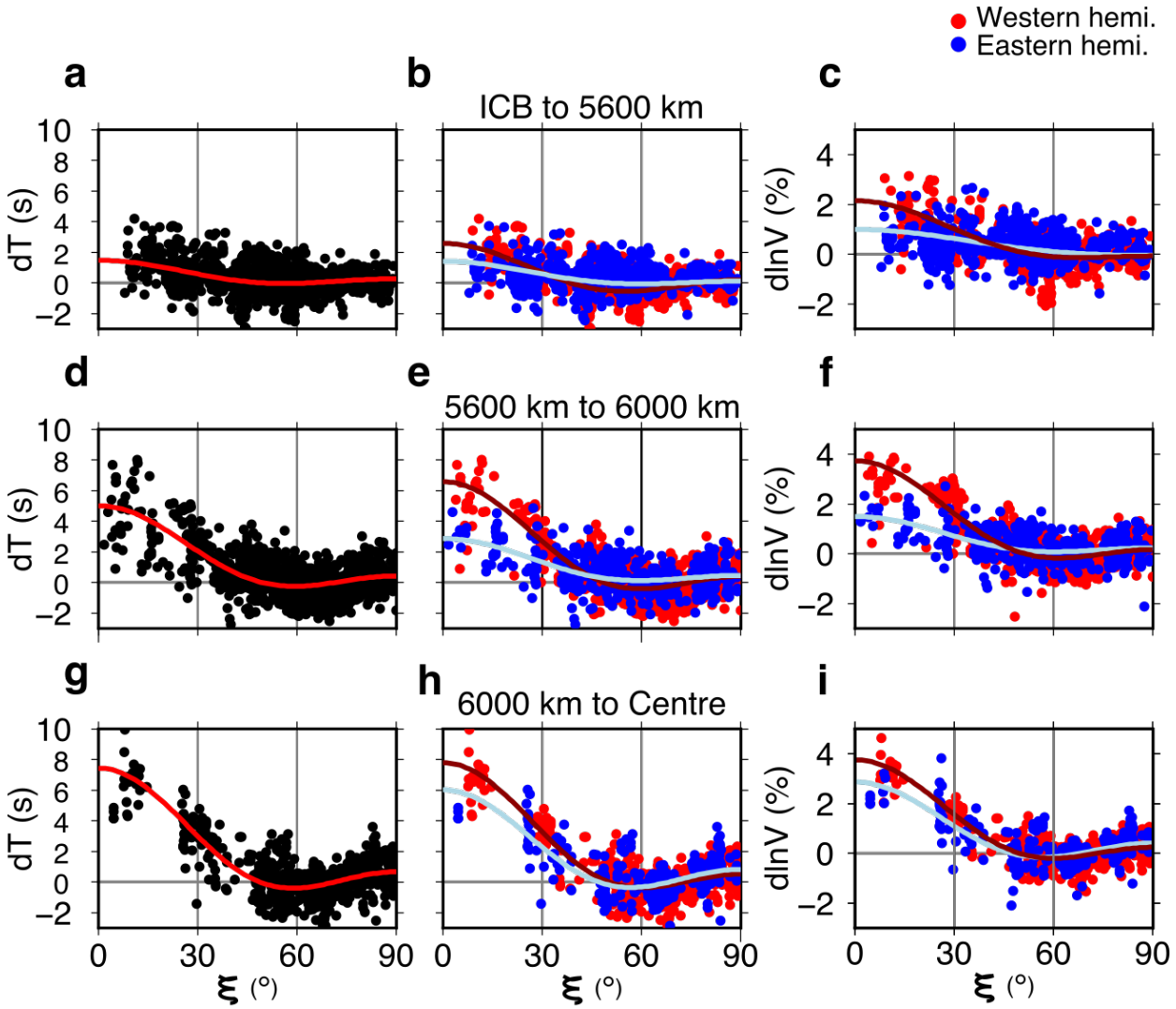

Extended Data Figure 4: Differential travel times as a function of angle to the rotation axis, ξ, and depth. PKPbc-df and PKPab-df travel time anomalies and effective velocity anomalies (excluding the data recorded at stations in Alaska) as a function of angle ξ with respect to the rotation axis, separated by ray turning depth for (**a**, **b, and c**) ICB to 5600 km, (**d, e, and f**) 5600 km to 6000 km, and (**g, h, and i**) 6000 km to Earth's centre. (**a, d, g**): All travel time anomalies. (**b, e, h**) Travel time anomalies split into data turning in the western (red) and eastern (blue) hemispheres. (**c, f, i**) Effective velocity anomalies in the IC split by hemisphere. The WH western boundary is set at -159° E, and the WH eastern boundary is set at 40° E, as explained in Extended Data Figure 5.

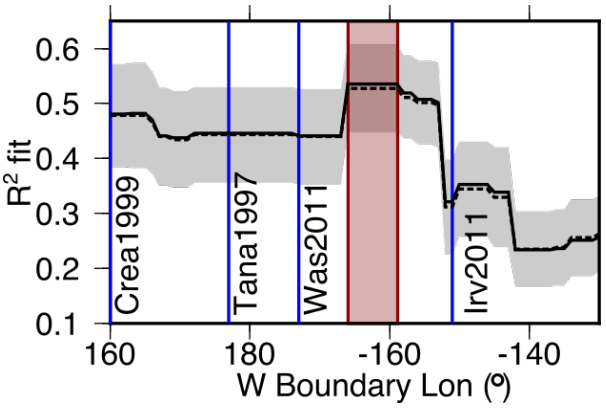

Extended Data Figure 5: Locating the western boundary of the western hemisphere. Best fit of WH western boundary locations calculated using polar data (ξ <15°) and excluding data from stations in Alaska. Black solid line marks the R^2 fit and red region describes the region of highest R^2, most likely containing the location of the boundary, which runs between -166° E and -159° E. R^2 drops sharply at <-166° E and >-153° E. Black dashed line and grey shading show the mean and standard deviation of R^2 values for 200 bootstrap resamples. The eastern boundary is fixed at 40°E, following the result of Irving (2016). Western boundary locations from previous studies are marked in blue: Tanaka & Hamaguchi 1997[6]; Creager 1999[7]; Waszek et al. 2011[74]; Irving & Deuss 2011[8]; while that of Lythgoe et al. 2014[9] plots outside of the region shown.

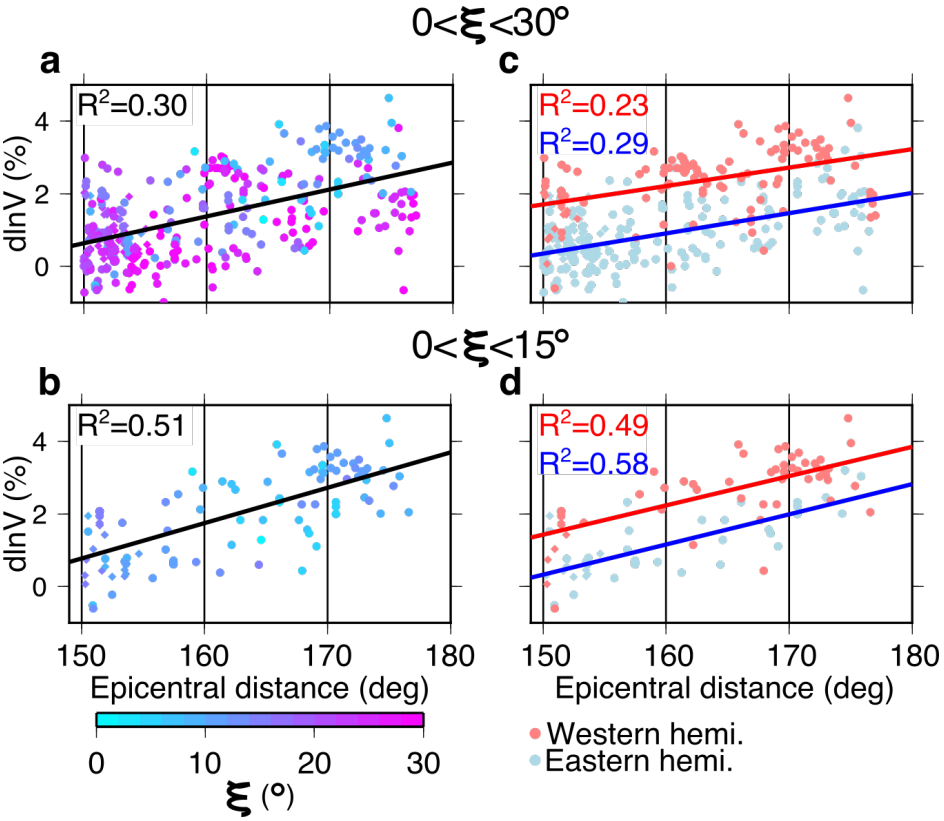

Extended Data Figure 6: Pattern of effective velocity anomaly with depth. Effective velocity anomaly in the IC as a function of epicentral distance for ξ in the range (**a** and **c**) 0 to

30°, and (**b** and **d**) 0 to 15°. Left panels show data coloured by ξ, and right panels show data split into those turning in the eastern (blue) and western (red) hemispheres. The western hemisphere is defined as between -159° E and 40° E, as explained in Extended Data Figure 5. The linear trend with distance, solid line, is particularly clear for the most polar data (**c** and **f**), indicating increasing anisotropy with depth.

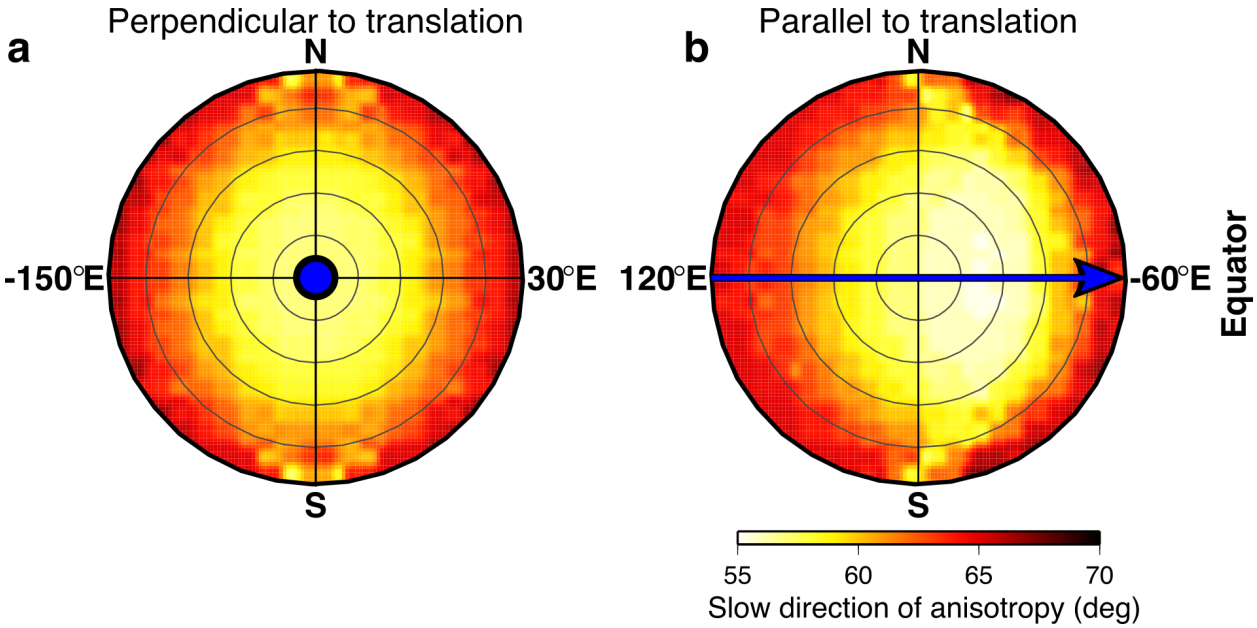

Extended Data Figure 7. Distribution of slow axes of anisotropy. Slow directions of anisotropy in our final model (Fig. 3), measured relative to the rotation (N-S) axis in the (**a**) plane perpendicular to the direction of translation (blue arrow coming out of plane), and (**b**) plane parallel to the direction of translation (blue arrow) from the left (east) to right (west) of the figure, respectively.

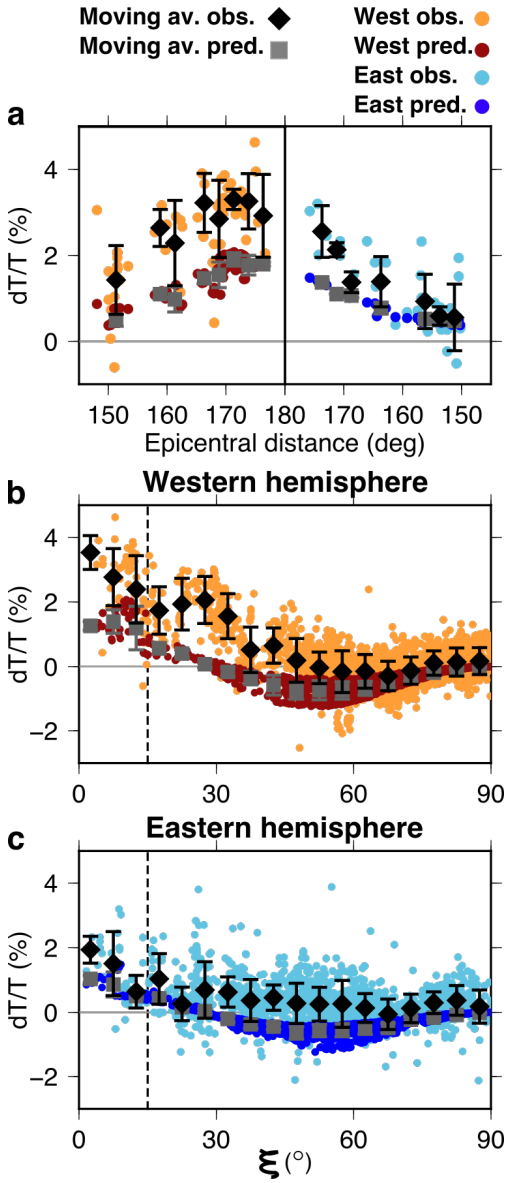

Extended Data Figure 8: Predicted versus observed PKP velocity anomalies for pure hcp Fe. Predicted (dark blue and red dots and with mean as grey squares) and observed (light blue and orange dots and with mean as black diamonds) effective velocity anomalies as a function of **(a)** epicentral distance for data with ξ≤15°, marked by dashed line in **b** and **c**, and as a function of ξ in the **(b)** western and **(c)** eastern hemispheres. Error bars for the data show the mean and one standard deviation at 2.5° and 5° increments for panels **a,** and **b** and **c**, respectively. We use the elastic tensor for pure HCP Fe at 5500 K and 360 GPa[68], an age of 0.5 Ga, and a translation rate of 0.3 radii over the age of the IC. Variance reduction for the data with ξ<15° is 73% compared to 93% for our model with $Fe_{93.25}Ni_{6.75}$.

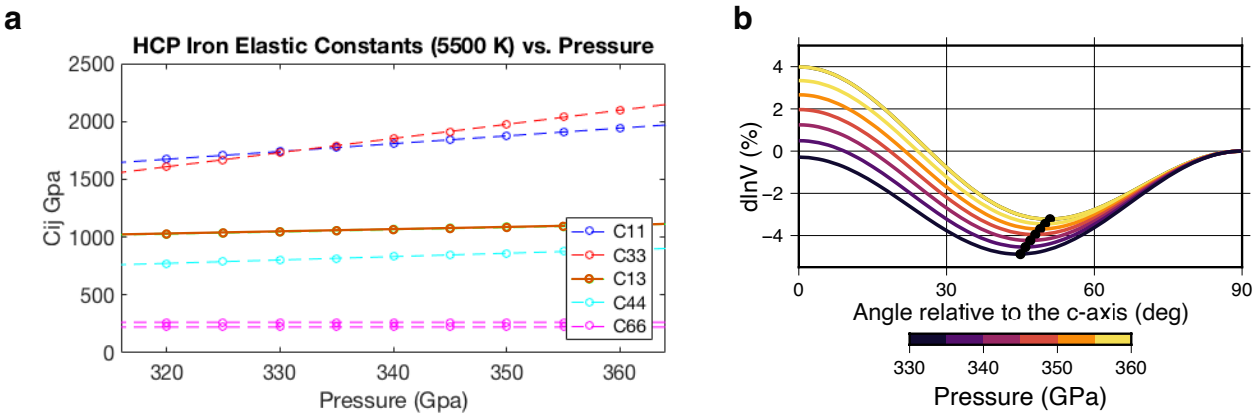

Extended Data Figure 9: The effect of pressure on anisotropy. (a) Elastic constants for hcp iron as a function of pressure calculated from the reference position at 360 GPa and 5500 K, extrapolated using results from several calculations[59,68] at 5500 K and 316 GPa, and 5500 K and 360 GPa. (**b**) Resultant anisotropy across the pressure range of the inner core. Direction of minimum velocity anomaly is marked by black circles. The orientation of the minimum anisotropy moves towards higher ξ values (more equatorial) with increasing pressure.